Published in: IEEE Wireless Communications Letters, May 2025. DOI: 10.1109/LWC.2025.3542564

Reflection Modeling of Modular Passive IRS Geometries

Simon Häger, Stefan Böcker, and Christian Wietfeld

***Abstract*—Intelligent reflecting surfaces (IRSs) will be key for efficient ubiquitous 6G millimeter-wave (mmWave) connectivity. Geometry-defined static IRSs following the *HELIOS* architecture could be adopted in the short term owing to scalability and compatibility with current generation networks. They need to be custom-tailored to the deployment scenario, however, reliance on electromagnetic (EM) simulations is a time-consuming bottleneck during the geometry optimization stage. Therefore, this letter introduces and validates an analytical reflection model based on physical optics (PO). Our findings demonstrate that the reflection pattern is accurately estimated, particularly within and around the main lobe, while significantly reducing computation time.**

***Index Terms*—Intelligent reflecting surface, reflection model, mmWave communications, radar cross section, EM simulation.**

I. Geometry-defined IRSs for 6G mmWave

FUTURE 6G networks are expected to operate millimeter-wave (mmWave) cells for ultra-high connectivity to accommodate growing data traffic. Compared to traditional sub-6 GHz communications, coverage is smaller with more shadow regions within, owing to challenging propagation characteristics. The deployment of extra full-blown base stations (BSs) to illuminate under-connected non-line-of-sight (NLOS) areas would be costly. Passive intelligent reflecting surfaces (IRSs) have emerged as a promising solution for efficiently improving connectivity by dynamically reflecting incident mmWaves to nearby user equipment (UEs) [1, 2]. Although prototypes show promise, challenges such as scalable size, channel estimation, and control signaling require further development [3]. Static realizations instead exhibit a preconfigured reflection making them cost-efficient and, in particular, compatible with current-generation networks. Their custom-tailored reflection pattern allows for stable delivery of quality of service (QoS)-compliant connectivity in the intended service area [4, 5].

Against this background, we proposed the *Holistic Enlightening of bLackspots with passIve reflectOr moduleS* (HELIOS) concept [6] which combines additive manufacturing and conductive coating, cf. Fig. 1. The modular approach allows for both scalability and parametrizability, with the combined geometry determining the overall reflection characteristics, e.g., in terms of reflection direction, beamwidth, and gain [6–8]. Measurement campaigns have confirmed that such custom-tailored reflectors boost connectivity as intended [4, 6, 9]. However, the iterative optimization process which shapes the geometry according to the target reflection characteristics leverages time-consuming electromagnetic (EM) simulations which delay production and deployment by days [9]. The key contribution of this work resolves this operational bottleneck by developing an accurate analytical reflection model based on the physical optics (PO) technique [10]. Comparisons against EM simulations validate its high accuracy and observe more than three orders of magnitude shorter computation time.

The remainder of this letter is organized as follows. Sec. II discusses analytical reflection models for optimized mmWave networks using customized static IRSs following the geometric HELIOS approach. We derive the analytical model in Sec. III, which is subsequently validated against EM simulations in Sec. IV. Last, Sec. V summarizes the key results of this letter.

Manuscript received Sep. 26, 2024; revised Dec. 20, 2024; accepted Feb. 10, 2025. Date of publication Feb. 17, 2025; date of current version Feb. 13, 2025. This work was supported by the German Federal Ministry of Education and Research (BMBF) in the course of the *6GEM Research Hub* under the grant number 16KISK038. The associate editor coordinating the review of this manuscript and approving it for publication was Yun Hee Kim. *(Corresponding author: Simon Häger).*

The authors are affiliated with the Communication Networks Institute (CNI) at TU Dortmund University, 44227 Dortmund, NRW, Germany. E-mail: {Simon.Haeger, Stefan.Boecker, Christian.Wietfeld}@tu-dortmund.de.

Digital Object Identifier 10.1109/LWC.2025.3542564

II. Preliminaries: IRS-based Channel and HELIOS

This section reviews preliminaries, starting in Sec. II-A with a beyond line-of-sight (LOS) channel model that integrates IRS reflection characteristics. Thereafter, Sec. II-B provides a detailed introduction to the HELIOS reflector architecture.

A. Channel Modeling with Reflecting Surfaces

The received power P_{RX} of a LOS link from the transmitter (TX) to the receiver (RX) is simply described by the free-space formula, which depends on distance $d_{\mathrm{TX,RX}}$, wavelength λ, transmit power P_{TX}, and respective antenna gains G [11]. Obstructions reduce P_{RX} further but static-passive IRSs can

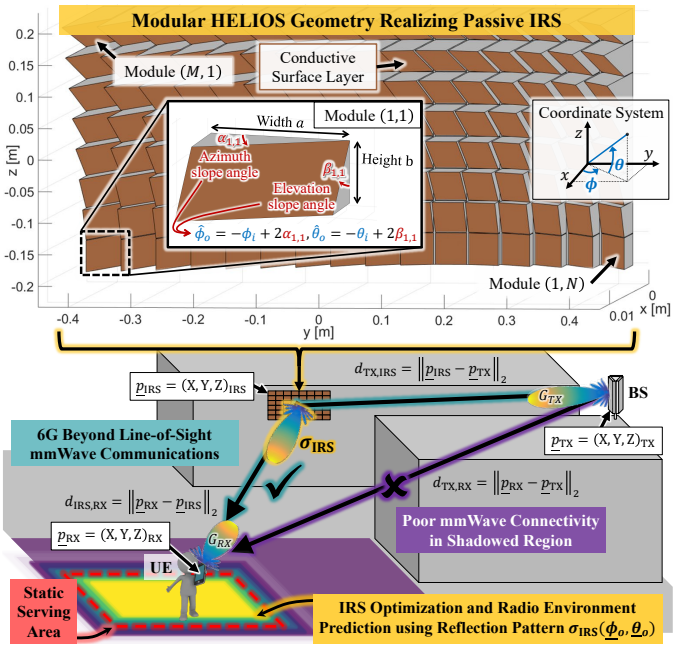

Fig. 1. Downlink transmission to NLOS UE via HELIOS IRS. The proposed reflection model is key for a future efficient reflector configuration process.

recover these losses [12]. Mounted at a suitable position and orientation, the given incident EM wave from the TX is reflected with gain σ_{IRS} to the RX. In literature, σ_{IRS} is referred to as the bistatic radar cross section (RCS) with unit m^2 (logarithmically: dBsm). Using the geometric relations from the bottom of Fig. 1, we can apply the radar equation [11].

$$P_{\text{RX}} = \frac{P_{\text{TX}} \cdot G_{\text{TX}} \cdot G_{\text{RX}} \cdot \sigma_{\text{IRS}} \cdot \lambda^2}{(4\pi)^3 \cdot d_{\text{TX,IRS}}^2 \cdot d_{\text{IRS,RX}}^2} \tag{1}$$

This channel model can be used in the scope of network planning to identify the QoS targets for the reflector design process, i.e., the required gain σ_{IRS} for a set of users at various distances and, in particular, azimuth and elevation reflection angles $(\phi_o, \theta_o) \in [-90°, 90°]^2$ from the considered mounting position. A reflection model may now be used to determine a QoS requirements-compliant IRS design for deployment.

For example, Özdogan *et al.* [13] consider an IRS that reflects the incident wave from direction γ_i in an idealized beamforming-like manner towards the configured steering direction $\gamma_{o,sd}$. Their model assumes an $M \times N$ array of synthetic unit cells of size $a \times b$ with $a, b < \lambda$. The reflection pattern $\sigma_{\text{IRS}}\left(\gamma_{o,od} \mid \gamma_i, \lambda, N, a, M, b, \gamma_{o,sd}\right)$ arises in dependence on the observation direction $\gamma_{o,od}$ [13]. We note that other models, e.g., [1, 2], extend it by proportionality to the reflectance $\Gamma^2 \in [0, 1]$ of the surface material. In this work, we implicitly assume $\Gamma^2 = 1$, i.e., a perfect reflecting surface without material loss which approximates copper and silver [14]. Moreover, more complex models by Tang *et al.* [2] and ours in Sec. III allow for assessment of the reflection pattern for arbitrary IRS configurations, which is useful if customized behavior, such as a broad reflection beam, is desired by coupling with an optimizer [9]. Nonetheless, the presented models can be fed into Eq. (1) to determine the impact of the IRS on more than the desired service area. Hence, they are essential for hybrid network planning aiming to jointly optimize BS and IRS deployment for efficient mmWave networks.

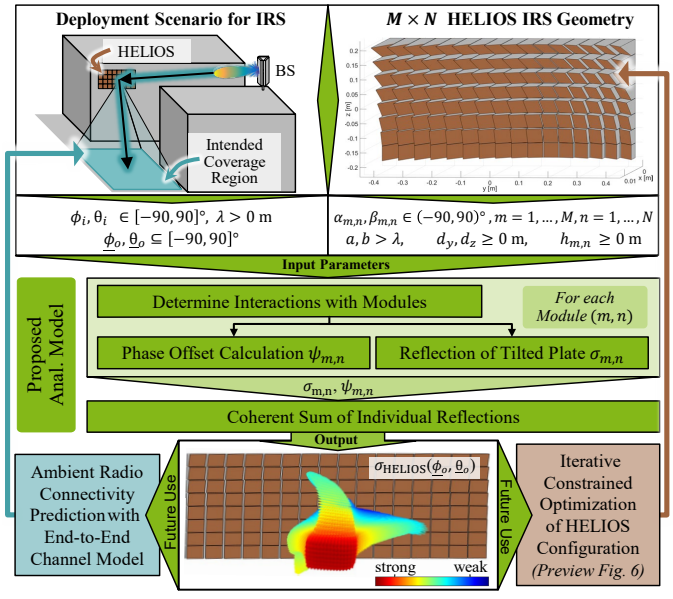

Fig. 2. Flowchart for the fast estimation of the reflection characteristics of a given HELIOS reflector geometry, allowing for connectivity prediction within the considered deployment scenario and iterative passive IRS optimization.

B. Geometry-defined IRSs for Custom-tailored Connectivity

Static passive IRSs benefit from mitigated control signaling and power consumption [1]. However, synthetic realizations for mmWave carriers are still in their infancy owing to, e.g., design complexity and scalability problems. Tilted and curved metallic surfaces can also provide the desired reflection [1, 12], with modular designs offering easier customization and scalability, while maintaining high geometric flexibility [6–8].

One such solution is HELIOS [6] leveraging 3D-printed modules with conductive varnish, see Fig. 1. They are arranged as a uniform $M \times N$ array in the y-z-plane. Each module has a footprint size of $a \times b$ $(a, b > \lambda)$ and is defined by the horizontal and vertical slope angles α, β that describe the 3D tilt of the reflecting surface. Accordingly, the incident wave from direction (ϕ_i, θ_i) is reflected towards azimuth and elevation angles $\hat{\phi}_o = -\phi_i + 2\alpha$ and $\hat{\theta}_o = -\theta_i + 2\alpha$. Further degrees of freedom are the adjustable socket heights $h_{m,n} \geq 0\,\text{m}$ as well as horizontal and vertical inter-module spacings $d_y, d_z \geq 0\,\text{m}$.

However, the assessment of the reflection pattern of a geometry-defined IRS currently depends on time-consuming EM simulations, constituting a bottleneck for the deployment of scenario-tailored mmWave reflectors, as noted in [9]. Therefore, this letter contributes an analytical reflection model for integration into 6G network planning, as shown in Fig. 2. We note that it is also directly applicable to other geometry-driven reflector approaches, for example, the two presented in [7, 8].

III. Proposal of Reflection Model

This section presents our analytical model for the reflection behavior of HELIOS. First, Sec. III-A derives the reflection pattern of a single IRS module. It is then extended in Sec. III-B to HELIOS arrays accounting for self-shadowing effects. The limitations of the proposed model are discussed in Sec. III-C.

A. Reflection Pattern of a Tilted Reflecting Surface

Similar to the IRS model in Sec. II-A, we build up on the reflection behavior of rectangular metallic surfaces. There are various models, e.g., [11, Ch. 6.3], [10, Ch. 11.3], [15, Ch. 9.1], and [16, Ch. 11.3], which are based on PO techniques. They differ by the assumed polarization and coordinate systems. Importantly, they are limited to special cases where at least one variable of $\phi_i, \theta_i, \phi_o, \theta_o$ is fixed [10, 11, 16], or some angular impact on the magnitude is ignored [15]. Thus, we derive the general RCS of a plate based on the EM theory in [10, Chapters 6.8, 7.11] and adapt it to a HELIOS module.

Flat Plate: The coordinate system from Fig. 1 is used with

$$\underline{r}\,(\phi, \theta) = [\cos\phi\cos\theta,\ \sin\phi\cos\theta,\ \sin\theta]^T \tag{2}$$

describing the position $\underline{p} = [x, y, z]^T$ of an object relative to the reflecting surface. It has a size of $a \times b$ in the y-z-plane with normal vector $\underline{n} = \underline{e}_x = [1, 0, 0]^T$. In the following derivation, we use the wave number $k = 2\pi/\lambda$ and the E-field magnitude $E_0 = Z_w H_0$, with the latter being defined by H-field magnitude H_0 and intrinsic impedance $Z_w = \sqrt{\mu_0/\epsilon_0}$. Against this background, we assume the following transverse incident E- and H-fields along the unit vectors of the spherical coordinate system that are mutually orthogonal to $-\underline{r}\,(\phi_i, \theta_i)$:

$$\underline{E}_i = \begin{bmatrix} E_x \\ E_y \\ E_z \end{bmatrix} = Z_w H_0 \begin{bmatrix} \sin\phi_i \\ -\cos\phi_i \\ 0 \end{bmatrix} e^{j\cdot k\cdot\langle \underline{p},\underline{r}(\phi_i,\theta_i)\rangle} \quad (3)$$

$$\underline{H}_i = \begin{bmatrix} H_x \\ H_y \\ H_z \end{bmatrix} = H_0 \begin{bmatrix} -\cos\phi_i \sin\theta_i \\ -\sin\phi_i \sin\theta_i \\ \cos\theta_i \end{bmatrix} e^{j\cdot k\cdot\langle \underline{p},\underline{r}(\phi_i,\theta_i)\rangle} \quad (4)$$

Therefore, the current $\underline{J} = 2\underline{n} \times \underline{H}_i|_{x=0}$ is induced in the rectangular metal plate and used by PO techniques to approximate the scattered E-field magnitude at distance r by [10]

$$E_s \simeq \frac{-j\cdot k\cdot Z_w}{4\pi\cdot r} \cdot \left(N_\phi\left(\underline{J}\right) + N_\theta\left(\underline{J}\right)\right) \cdot e^{j\cdot k\cdot\langle \underline{p},\underline{r}(\phi_o,\theta_o)\rangle} \text{ with } (5)$$

$$\underline{J} = \begin{bmatrix} J_x \\ J_y \\ J_z \end{bmatrix} = 2H_0 \begin{bmatrix} 0 \\ -\cos\theta_i \\ -\sin\phi_i \sin\theta_i \end{bmatrix} e^{j\cdot k\cdot(y\sin\phi_i\cos\theta_i + z\sin\theta_i)}. \quad (6)$$

To calculate the two new terms in Eq. (5), and for later use in Sec. III-B, we introduce these three terms as in [15, Ch. 9.1]:

$$X = k\cdot(\cos\phi_o\cos\theta_o + \cos\phi_i\cos\theta_i) \quad (7)$$

$$Y = k\cdot(\sin\phi_o\cos\theta_o + \sin\phi_i\cos\theta_i)\cdot a/2 \quad (8)$$

$$Z = k\cdot(\sin\theta_o + \sin\theta_i)\cdot b/2 \quad (9)$$

Using Eqs. (6), (8) and (9), we determine N_ϕ and N_θ [10]:

$$\begin{aligned} N_\phi &= \int_{-a/2}^{a/2}\int_{-b/2}^{b/2} (-J_x\sin\phi_o + J_y\cos\phi_o) \\ &\quad \cdot e^{j\cdot k\cdot(y\sin\phi_o\cos\theta_o + z\sin\theta_o)} dz dy \\ &= -2H_0\cos\theta_i\cos\phi_0 \cdot \int_{-b/2}^{b/2} e^{j\cdot k\cdot z\cdot(\sin\theta_o+\sin\theta_i)} dz \\ &\quad \cdot \int_{-a/2}^{a/2} e^{j\cdot k\cdot y\cdot(\sin\phi_o\cos\theta_o+\sin\phi_i\cos\theta_i)} dy \\ &\overset{Eq.\ (12)}{=} -2H_0\cdot a\cdot b\cdot \operatorname{sinc} Y\cdot\operatorname{sinc} Z\cdot\cos\phi_o\cos\theta_i \end{aligned} \quad (10)$$

$$\begin{aligned} N_\theta &= \int_{-a/2}^{a/2}\int_{-b/2}^{b/2} (J_x\sin\theta_o\cos\phi_o + J_y\sin\theta_o\sin\phi_o \\ &\quad - J_z\cos\theta_o)\cdot e^{j\cdot k\cdot(y\sin\phi_o\cos\theta_o + z\sin\theta_o)} dz dy \\ &\overset{Eq.\ (12)}{=} -2H_0\cdot a\cdot b\cdot\operatorname{sinc} Y\cdot\operatorname{sinc} Z \\ &\quad \cdot(\cos\theta_i\sin\theta_o\sin\phi_o - \sin\phi_i\sin\theta_i\cos\theta_o) \end{aligned} \quad (11)$$

$$\int_{-c/2}^{c/2} e^{j\cdot u\cdot x} dx = \frac{e^{j\cdot u\cdot c/2} - e^{-j\cdot u\cdot c/2}}{j\cdot u} \overset{*}{=} c\cdot\operatorname{sinc}\left(\frac{c\cdot u}{2}\right) \quad (12)$$

The RCS may now be determined based on its definition [10]:

$$\sigma_{\text{Plate}} = \lim_{r\to\infty} 4\pi r^2 \frac{|E_s|^2}{|E_0|^2} = 4\pi\left(\frac{a\cdot b}{\lambda}\cdot\operatorname{sinc} Y\cdot\operatorname{sinc} Z\cdot T\right)^2, \quad (13)$$

where T bundles the angular factors contained in N_ϕ, N_θ with

$$\begin{aligned} T = &-\cos\theta_i\cos\phi_o - \cos\theta_i\sin\theta_o\sin\phi_o \\ &+ \sin\phi_i\sin\theta_i\cos\theta_o. \end{aligned} \quad (14)$$

We note a symmetric up- and downlink behavior of $\operatorname{sinc} Y$, $\operatorname{sinc} Z$, and T when interchanging (ϕ_i,θ_i) with $(-\phi_o,-\theta_o)$.

HELIOS module: Eq. (13) represents only a flat HELIOS module with slope angles $\alpha,\beta = 0°$. However, when tilting the reflecting surface, the local coordinate system is rotated by

$$\phi_i^r = \phi_i - \alpha,\ \phi_o^r = \phi_o - \alpha \text{ and } \theta_i^r = \theta_i - \beta,\ \theta_o^r = \theta_o - \beta. \quad (15)$$

* We employ $\operatorname{sinc}(x) = \sin(x)/x$ with $\operatorname{sinc}(0) := \lim_{x\to 0}\operatorname{sinc}(x) = 1$.

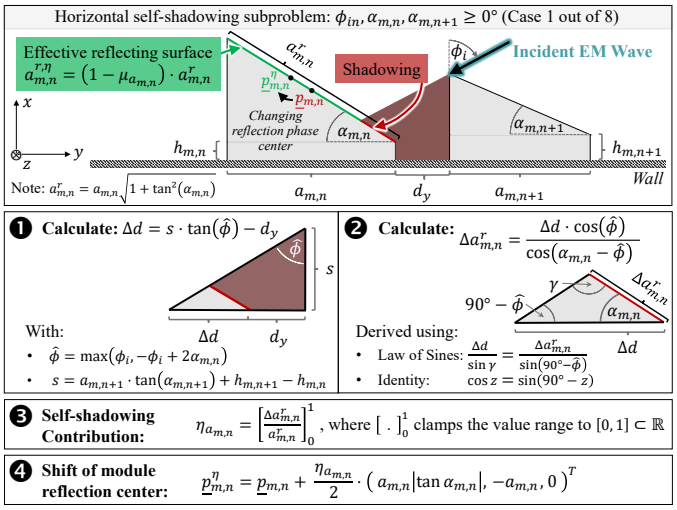

Fig. 3. Sample calculation of horizontal self-shadowing contribution $\eta_{a_{m,n}}$ in three steps, followed by an update of the module's reflection center $\underline{p}^\eta_{m,n}$. Similar calculations apply to the other seven cases and vertical self-shadowing.

The side lengths of the reflecting surface further increase to

$$a^r = a\cdot\sqrt{1+\tan^2(\alpha)} \text{ and } b^r = b\cdot\sqrt{1+\tan^2(\beta)}. \quad (16)$$

Substituting the transformations in Eqs. (15) and (16) for the variables $a, b, \phi_i, \phi_o, \theta_i, \theta_o$ in Eq. (13), including Eqs. (8), (9) and (14), yields the module reflection pattern $\sigma_{m,n}(\phi_o,\theta_o)$.

B. Extension to Array of Reflecting Surfaces

***M*×*N* Module Array:** The superposition of reflections $\sigma_{m,n}$ requires the calculation of the reflection centers, e.g.,

$$\underline{p}_{m,n} = \begin{bmatrix} \frac{a}{2}\cdot|\tan\alpha_{m,n}| + \frac{b}{2}\cdot|\tan\beta_{m,n}| + h_{m,n} \\ \frac{2n-1-N}{2}\cdot a + \frac{2(n-1)-(N-1)}{2}\cdot d_y \\ \frac{2m-1-M}{2}\cdot b + \frac{2(m-1)-(M-1)}{2}\cdot d_z \end{bmatrix} \quad (17)$$

with $m = 1,\ldots,M$ and $n = 1,\ldots,N$. Consequently, the phase offsets $\psi_{m,n}$ against the IRS's origin are identified via

$$\psi_{m,n} = \left\langle \underline{p}_{m,n}, [X, Y\cdot 2/a, Z\cdot 2/b]^T \right\rangle, \quad (18)$$

using Eqs. (7) to (9) without the transformation in Eq. (15). Against this background, the overall reflection characteristic is finally determined using the coherent sum [16, Ch. 11.3]

$$\sigma_{\text{HELIOS}} = \left| \sum_{m=1}^{M}\sum_{n=1}^{N} \left(\sqrt{\sigma_{m,n}}\cdot e^{j\cdot\psi_{m,n}}\right)\right|^2. \quad (19)$$

Self-shadowing: Certain HELIOS parametrizations may cause the reflecting surface of module (m,n) to be partially obstructed by some neighboring modules. It holds $\underline{J} \approx 0$ in shaded areas [10, 16]. Consequently, *(i)* the reflecting surface area $a^r_{m,n}\times b^r_{m,n}$, see Eq. (16), and *(ii)* the reflection center $\underline{p}_{m,n}$, see Eq. (17), need to be adapted for high accuracy.

The self-shadowing contains horizontal and vertical contributions $\eta_{a_{m,n}}, \eta_{b_{m,n}} \in [0,1]$ yielding the correction terms

$$a^{r,\eta}_{m,n} = a^r_{m,n}\left(1-\eta_{a_{m,n}}\right) \text{ and } b^{r,\eta}_{m,n} = b^r_{m,n}\left(1-\eta_{b_{m,n}}\right). \quad (20)$$

They are determined independently using similar formulas

owing to symmetry. $\eta_{a_{m,n}}$ depends on the parameter sextuple $(\phi_i, \alpha_{m,n}, \alpha_{m,n+1}, d_y, h_{m,n}, h_{m,n+1})$, whereas $\eta_{b_{m,n}}$ on $(\theta_i, \beta_{m,n}, \beta_{m+1,n}, d_z, h_{m,n}, h_{m+1,n})$. The exact formula depends on the signs ($\geq 0 / < 0$) of the respective three key parameters $(\alpha_{m,n}, \alpha_{m,n+1}, \phi_i)$ or $(\beta_{m,n}, \beta_{m+1,n}, \theta_i)$. Hence, there are eight (2^3) formulas. For brevity, Fig. 3 derives one of them in the context of the horizontal self-shadowing contribution: $\eta_{a_{m,n}}$ is calculated in three steps for the first case wherein $\alpha_{m,n}, \alpha_{m,n+1}, \phi_i \geq 0°$. It can be seen that the result moreover depends on parameters $d_y, h_{m,n}$, and $h_{m,n+1}$ which, if intelligently selected, allow for mitigation of the horizontal self-shadowing. We further note that the fourth step in Fig. 3 subsequently outlines how the reflection center $\underline{p}_{m,n}$ is updated by $\underline{p}^{\eta}_{m,n}$ to account for the horizontal shadowing. As mentioned previously, the vertical shadowing contribution $\eta_{b_{m,n}}$ and its impact on the reflection center can be calculated analogously.

C. Notes on Applicability of the Proposed Reflection Model

(i) The PO technique is suitable for high carrier frequencies. Moreover, high accuracy is expected if the surface dimensions a^r and b^r exceed the wavelength λ by factor five or more [10, 15]. It is therefore rather suitable for the mmWave than sub-6 GHz spectrum as the overall IRS footprint could become too large for some deployment scenarios. *(ii)* The determined reflection characteristics and their integration into end-to-end channel models, cf. Eq. (1), are only applicable if TX and RX are in the far field of the passive IRS [10, 13], i.e., if

$$d_{\text{TX,IRS}}, d_{\text{IRS,RX}} \geq \frac{2}{\lambda} \cdot \max\left(\left(N \cdot a + (N-1) \cdot d_y\right)^2, \left(M \cdot b + (M-1) \cdot d_z\right)^2 \right). \quad (21)$$

Hence, even if the BS is in the far field, for larger IRSs it becomes increasingly likely that RXs might be in the near field wherein the modeled far-field reflection characteristic may only be partially applicable. A near-field extension of the proposed model would particularly need to employ module-specific reflection angles $\phi_{o_{m,n}}, \theta_{o_{m,n}}$ to the close-by UE. *(iii)* It is noted that complex EM wave interactions, such as multiple reflections or edge diffraction, are not accounted for.

IV. Validation against EM Simulations

This section systematically validates the proposed analytical reflection model for HELIOS against EM simulation results using the RCS solver of Ansys HFSS, as in prior works [6, 9].

We first study the reflection patterns of individual HELIOS modules in Fig. 4 for different *(a)* tilt angles, *(b)* surface sizes, and *(c)* frequencies. It is confirmed in *(a)* that the reflection angle changes proportionally to the tilt angle. In *(b)* and *(c)* it is observed that the directionality of the reflection increases with the module size and carrier frequency, respectively. A good match is observed in the main lobe as well as the first- and second-order side lobes, with less than 0.01 dB error between EM simulations and the proposed reflection model. Considering Fig. 4a closely, it can be seen that a mismatch appears towards the edge, i.e., far away from the specular reflection direction, with the model underestimating the RCS by up to 10 dB. However, this is a typical behavior of the leveraged PO approach, cf. [16, Ch. 11.2]. Importantly, with the error being far from the main lobe, the future model-based configuration process realizing custom reflection beams shall not be adversely affected. We thus summarize that our analytical derivation from Sec. III-A has been successfully validated.

Second, the coherent sum of the individual reflections is validated using multiple modules. Fig. 5a shows that the peak gains match well regardless of the number of modules and the array shape. We further consider the entire horizontal reflection pattern in Fig. 5b for the 1×2 case *(left)* without and *(right)* with module spacing d_y. Again, the reflection patterns of model and simulations match for $|\phi_o| \ll 90°$. Moreover, the results underline the potential of inter-module spacings d_y, d_z for future reflection pattern optimization, as the side lobe level and its spacing to the main lobe are affected. We thus conclude that our contribution outlined in Sec. III-B has been validated specifically for the case that no self-shadowing occurs.

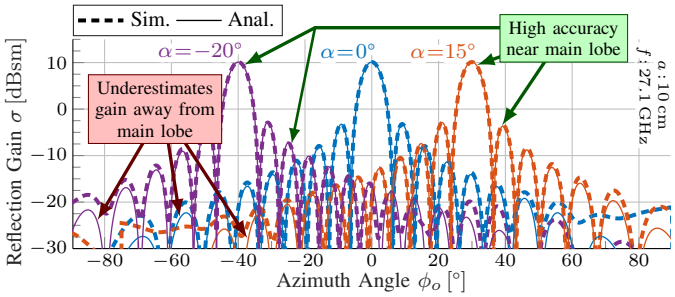

(a) Reflection angle depends on configured slope angle α.

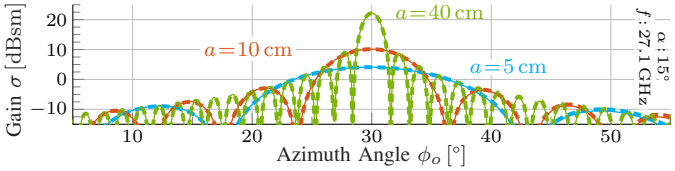

(b) Higher gain by larger module width a at cost of smaller beamwidth.

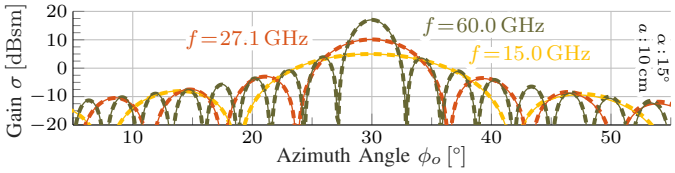

(c) More directional reflection of fixed-size module at higher frequency f.

Fig. 4. Multivariate comparison between simulated and modeled reflection of HELIOS modules. Horizontal-plane reflection slices ($\theta_o = 0°$) for EM wave impinging from $\phi_i, \theta_i = 0°$ match well. (Fixed: $b = 10\,\text{cm}, \beta = 0°$.)

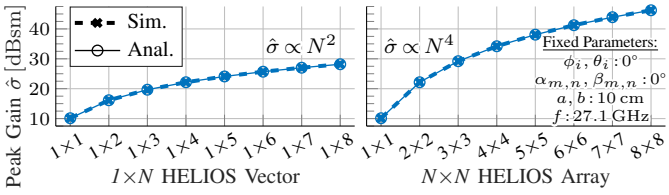

(a) Scalability analysis of peak reflection gain. Maximum error: 0.002 dB.

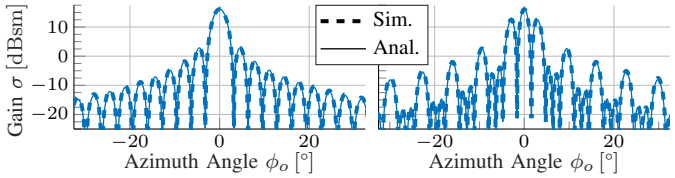

(b) Horizontal-plane reflection pattern slices ($\theta_o = 0°$) for 1×2 configuration: *(left)* without spacing ($d_y = 0\,\text{cm}$) and *(right)* with $d_y = 10\,\text{cm}$ spacing.

Fig. 5. Validating model for arrays of flat plates. No shadowing occurs.

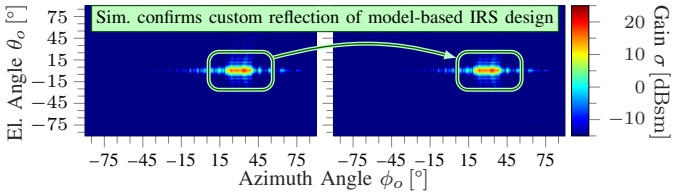

(a) Full reflection patterns: *(left)* proposed model, *(right)* EM simulation.

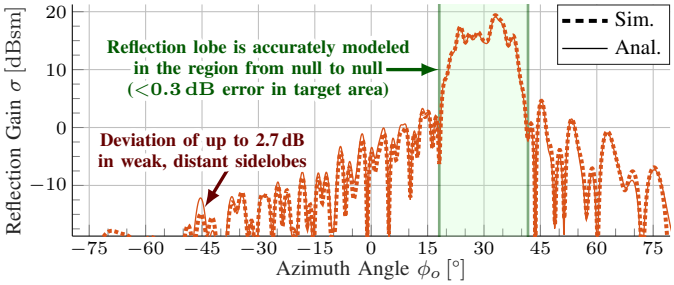

(b) Horizontally broadened reflection beam depicted at $\theta_o = 0°$.

Fig. 6. Comparing reflection of analytical model-based 3×3 HELIOS design against EM simulations. Genetic algorithm-based customization process realizes horizontally broadened reflection towards $\phi_o \in [25°, 35°]$. (Fixed: $\phi_i, \theta_i = 0°$, $a, b = 10\,\text{cm}$, $f = 29.5\,\text{GHz}$, $d_y, d_z, h_{m,n} = 0\,\text{m}$.)

TABLE I
MEAN COMPUTATION TIME OF $M \times N$ HELIOS REFLECTION PATTERN.

Configuration	Angular Resolution	EM Simulations (Ansys HFSS, 128 Cores)		Analytical Model (MATLAB, 1 Core)
1×1	1.00°	14.877 s	Factor: ≈ 14,900	0.001 s
1×1	0.50°	36.896 s		0.004 s
1×1	0.25°	117.311 s		0.024 s
1×1	0.10°	*(>15 min)* 1,026.735 s		0.149 s
2×2	1.00°	26.859 s		0.005 s
2×2	0.50°	81.947 s		0.016 s
2×2	0.25°	*(>5 min)* 337.937 s		0.088 s
2×2	0.10°	*(>30 min)* 2,017.616 s		0.563 s
4×4	1.00°	58.861 s		0.016 s
4×4	0.50°	180.377 s		0.054 s
4×4	0.25°	*(>10 min)* 663.346 s	Factor: ≈ 1,800	0.344 s
4×4	0.10°	*(>1 h)* 4,057.127 s		2.235 s

*Sample size 100: $\alpha_{m,n}, \beta_{m,n} = 0°, 1°, \ldots, 9°$. $f = 27.1\,\text{GHz}$; $a, b = 10\,\text{cm}$; $\phi_i, \theta_i = 0°$.

In contrast to the previous comparisons, the reflection of a custom-tailored HELIOS configuration that incurs self-shadowing is considered in Fig. 6. The 18 slope angle parameters $\alpha_{m,n}, \beta_{m,n}$ of the 3×3 IRS were identified in about 12,800 iterations using a genetic algorithm like in [9], however, in conjunction with the proposed reflection model. The simulated reflection pattern for the HELIOS, which is only coated in the non-shadowed regions, matches well with the analytical prediction, see Fig. 6a. Studying the horizontal-plane reflection slice of the broadened beam as shown with 0.1° resolution in Fig. 6b, deviations of less than 0.3 dB are observed around the reflection beam center at $\phi_o = 30°$. We can therefore confirm that the analytical IRS design shall perform as expected in practice. Again, the error increases at angles far from the main lobe region, however, they are insignificant for the showcased future IRS configuration use of the model due to the direction and magnitude of the deviations. Therefore, we summarize that the contribution of this letter, cf. Sec. III, has now been fully validated against EM simulations.

Last, we consider the computation time which made the EM simulations-based customization process in [9] infeasible, thus motivating this letter. Up to 3.2 million RCS values must be computed for full reflection patterns with $\phi_o, \theta_o \in [-90°, 90°]$ with 0.1° resolution. Tab. I shows that the mean simulation time scales with IRS size and angular resolution. A 4×4, $40\,\text{cm} \times 40\,\text{cm}$ IRS takes 67 min, whereas the proposed model completes in about 2.2 s, even without parallel computing techniques. A speedup of 14,900 is achieved for a single module, with the entire reflection being computed in 1 ms.

V. CONCLUSION

This letter presented an analytical reflection model for the geometry-driven passive HELIOS IRSs based on PO techniques. These methods are well-suited for the targeted mmWave spectrum and account for key EM wave characteristics, including interference and polarization. Comparisons with EM simulations showed a good match, particularly in the main lobe of the reflection pattern, with errors smaller than 0.3 dB. Moreover, computation time was reduced by more than three orders of magnitude. The proposed model is therefore a crucial enabler for our long-term goal of developing a hybrid network planner that identifies optimal IRS mounting positions and configurations for efficient 6G mmWave communications. To that end, our ongoing work adopts the model for a rapid QoS-conformal IRS customization process with additional constraints, including footprint minimization.

REFERENCES

[1] M. Di Renzo, F. H. Danufane, and S. Tretyakov, "Communication models for reconfigurable intelligent surfaces: From surface electromagnetics to wireless networks optimization," *Proc. IEEE*, vol. 110, no. 9, Sep. 2022.
[2] W. Tang *et al.*, "Wireless communications with reconfigurable intelligent surface: Path loss modeling and experimental measurement," *IEEE Trans. Wirel. Commun.*, vol. 20, no. 1, Jan. 2021.
[3] ETSI, "Reconfigurable intelligent surface; technological challenges, architecture and impact on standardization," GR 002 V1.1.1, Aug. 2023.
[4] M. Danger, C. Arendt, H. Schippers, S. Böcker, M. Mühleisen, P. Becker, J. B. Caro, G. Gjorgjievska, M. A. Latif, J. Ansari, N. Beckmann, N. König, R. Schmitt, and C. Wietfeld, "Performance evaluation of IRS-enhanced mmWave connectivity for 6G industrial networks," in *Proc. IEEE M&N Symp.*, Jul. 2024, Best Paper Young Author Award.
[5] G. Oliveri, F. Zardi, P. Rocca, M. Salucci, and A. Massa, "Constrained design of passive static EM skins," *IEEE Trans. Antennas Propag.*, vol. 71, no. 2, Feb. 2023.
[6] S. Häger, K. Heimann, S. Böcker, and C. Wietfeld, "Holistic enlightening of blackspots with passive tailorable reflecting surfaces for efficient urban mmWave networks," *IEEE Access*, vol. 11, Apr. 2023.
[7] J. S. Romero-Peña and N. Cardona, "Irregular multifocal reflector for efficient mmWave propagation in indoor enviroments," in *Proc. EuCAP Conf.*, Mar. 2020.
[8] K. Qian, L. Yao, X. Zhang, and T. N. Ng, "MilliMirror: 3D printed reflecting surface for millimeter-wave coverage expansion," in *Proc. ACM MobiCom Conf.*, Oct. 2022.
[9] S. Häger, M. Danger, K. Heimann, Y. Gümüs, S. Böcker, and C. Wietfeld, "Custom design and experimental evaluation of passive reflectors for mmWave private networks," in *Proc. IEEE LANMAN Symp.*, Jul. 2024, Best Paper Award.
[10] C. A. Balanis, *Advanced Engineering Electromagnetics*. Wiley, 2012.
[11] D. E. Kerr, S. A. Goudsmit, L. B. Linford, and A. M. Stone, Eds., *Propagation of Short Radio Waves*. IET, 1987.
[12] A. P. Ganesh *et al.*, "Propagation measurements and coverage analysis for mmWave and sub-THz frequency bands with transparent reflectors," in *Proc. IEEE VTC-Spring Conf.*, Jun. 2023.
[13] Ö. Özdogan, E. Björnson, and E. G. Larsson, "Intelligent reflecting surfaces: Physics, propagation, and pathloss modeling," *IEEE Wirel. Commun. Lett.*, vol. 9, no. 5, May 2020.
[14] E. A. Serov, V. V. Parshin, and G. M. Bubnov, "Reflectivity of metals in the millimeter wavelength range at cryogenic temperatures," *IEEE Trans. Microw. Theory Tech.*, vol. 64, no. 11, Nov. 2016.
[15] E. Björnson and Ö. T. Demir, *Introduction to Multiple Antenna Communications and Reconfigurable Surfaces*. Now Publishers, 2024.
[16] M. I. Skolnik, Ed., *Radar Handbook*. McGraw-Hill Professional, 2008.